Structural Health Monitoring of Bridges with Personal Laser Scanning: Segment-based Analysis of systematic Point Cloud Deformations

Robert Blaskow [1], Hans-Gerd Maas [1]

[1] Institute of Photogrammetry and Remote Sensing, Technische Universität Dresden, Germany
(robert.blaskow, hans-gerd.maas)@tu-dresden.de

Keywords: personal laser scanning, mobile mapping, segmentation, urban, digital twin, bridge monitoring

Abstract

Bridge structures can be surveyed using a number of different methods. Established are image-based methods using structure from motion by an unmanned aerial vehicle (UAV), terrestrial laser scanning (TLS), or a combination of both methods. Beyond static terrestrial laser scanning, buildings can also be efficiently surveyed using personal laser scanner (PLS) systems. The advantage here is the greater flexibility and increased speed compared to the static method. On the other hand, the accuracy may be more critical, and the resulting point cloud will be more sensitive to systematic global or local deformations under unfavorable measurement conditions. For example, temporary influences can lead to local mapping errors. These include influences such as uneven measurement system motion or non-static, feature-sparse environments.

This study investigates the acquisition of 3D point clouds representing the outer shell of a concrete bridge using a PLS system. We demonstrate a method for detecting possible deformations in PLS point clouds using the example of a bridge structure. For this purpose, the reference (TLS) and the PLS point clouds are segmented into individual clusters and a segment-based ICP fine registration is performed. Different RMSE values for the upper road section (0.061 m) and for the pillar segments (0.021 m) as well as different transformation parameters indicate slight displacements in the PLS point cloud. The analysis of the cloud-to-cloud distances showed that there were slight deformations in the Z direction in the area of the road surface. In the lateral direction, no significant residual deviations were found in the area of the bridge pillars.

1. Introduction

Structural health monitoring of bridges is performed for early detection of damage and to extend the service life. The basis are highly accurate three-dimensional geometric models of the corresponding buildings. Reconstruction from digitized 2D as build plans is one method of creating such models. Poku-Agyemang & Reiterer (2023) present an innovative workflow for digitizing bridges from 2D plans. Based on image processing for corner detection, 3D point cloud reconstruction of components, and fusion of reconstructed components, a true-to-scale 3D object can be created. In addition to the use of existing plan data, measurement data of the bridge structure can be acquired. Depending on the condition and accessibility of the bridge, different measurement methods can be used for data acquisition. Traditional single-point measurement methods such as tachymetry are used to measure discrete points. Haslbeck et al. (2022) use tachymeter and laser tracker generated data of bridge structures to explain and quantify the uncertainties inherent to geodetic observations. Alternatively, area-based surveying methods such as conventional photogrammetry, laser scanning or multi image based structure from motion methods can be used. The resulting 3D point clouds contain additional method-specific point attributes such as signal intensity or (multi-) spectral attributes. Previtali et al. (2022) present a methodology for creating a detailed building information model based on data from TLS systems, mobile mapping systems (MMS) and photogrammetry.

In addition to the measurement method, the choice of the measurement platform plays an important role in structural health monitoring of bridges. The use of UAVs, which can be deployed flexibly at different heights and over inaccessible terrain, is a good option. Mader et al. (2015) presented a concept in which a fleet of UAVs equipped with various sensors such as laser scanners, RGB cameras, near-infrared cameras and thermal cameras

inspect a bridge. It is also possible to use topo-bathymetric UAV-LiDAR systems to inspect the foundations of the pillars in or under water and the adjacent riverbed. Mandlburger et al. (2020) present a corresponding sensor concept. However, under the bridges themselves and in narrow river valleys, UAVs can face restrictions due to GNSS occlusions. For this case, Sardemann et al. (2023) developed an uncrewed water vehicle (UWV) that determines its position with photogrammetric methods from image sequences. This enables the underside of the bridge to be surveyed with LiDAR and the riverbed with an echo sounder.

Another category of mobile mapping systems are special SLAM-based PLS systems. Common systems use LiDAR, cameras, inertial measurement units (IMU) or in most cases a fusion of these sensors to generate the input data for the SLAM algorithm. Huang (2021) summarizes the development history and the function of the core modules of existing LiDAR based SLAM algorithms. In addition, state-of-the-art multi-sensor LiDAR SLAM techniques are examined and the future development trend of LiDAR SLAM is discussed.

The advantage of handheld or backpack-mounted PLS systems is the efficient and flexible mapping of wide areas or large structures. Compared to terrestrial laser scanning, PLS does not require static set ups, which leads to a higher acquisition speed, especially in complex measurement scenarios. Tupinambá-Simões et al. (2023) show that hand-held laser scanners (HLS) provide a fast and accurate way to map forest ecosystems. Aricò et al. (2023) demonstrate the potential of mapping a cultural heritage site using a HLS and particularly emphasize the temporal performance. For bridge monitoring, PLS systems are an easy-to-use and effective addition to established acquisition methods such as TLS and image-based UAV surveying. However, it should be noted that PLS point clouds can be systematically deformed as a consequence of the sequential operation of the SLAM algorithm

or by external influences during the measurement process, such as the measurement path or the object properties.

In this publication, we investigate the systematic deformations of a PLS point cloud of a two-lane concrete bridge using TLS reference measurements. Since the PLS point clouds can have locally varying deformations, a global point cloud comparison is not appropriate. Therefore, we present a novel segment-based approach for detecting local deformations in PLS point clouds. In the first step, the TLS and PLS point clouds are segmented into individual components based on the calculation of the geometric feature of the verticality factor. The individual segments of the bridge structure are then individually fine-registered to each other. In this manner, individual transformation matrices are obtained, which can already provide information about systematic deformations in the PLS point cloud. Finally, a segment-based point cloud deformation analysis is carried out by means of a point-to-point comparison. The methodical procedure is also validated using a synthetically transformed replica of the control point cloud.

The article is structured as follows. First, the study area and the method of data collection are explained, followed by details on the initial preparation of the data. The data processing method developed is then presented in detail. The results of the method applied to the recorded data are presented and discussed in the context of surveying a bridge. Finally, an outlook on potential future adaptations and a conclusion follow.

2. Study area and data acquisition

2.1 Study area

The object of investigation was a two-lane concrete bridge over a flood channel in Dresden, Germany (Figure 1). It was built in 2003/4 and has 5 spans with a total length of 140 meters. The height is 9 m and the width is 13 m. Due to the dry flood channel, the bridge was fully accessible at the time of the measurement. The site of the bridge is open with no attached buildings, the immediate surroundings consisted of meadows and vegetation such as bushes and trees. Vegetation was only present in the area of the abutments at road level.

Figure 1. Bridge "Sternstraße" Dresden

2.2 Field campaign for data acquisition

Geometric mapping focused on capturing the bridge as completely and as detailed as possible. To ensure the highest possible stability of the survey, the PLS path was chosen close to the bridge. The measurement data is georeferenced using control points. To have these automatically detected by the software, they must be integrated into the measurement by briefly setting up the scanner in a stationary position for at least 10 seconds. The control points were all at road level and distributed over the entire length of the bridge.

The PLS path started on the upper road level and continued to the lower level, where each pillar was surrounded by a partial loop. This was followed by a transition back to the upper level. The way back was along the pavement, with four changes of side for the control point measurement (Figure 2). The PLS track took about 14 minutes. Detailed information on the operation of PLS measurements can be found in Blaskow and Eltner (2023).
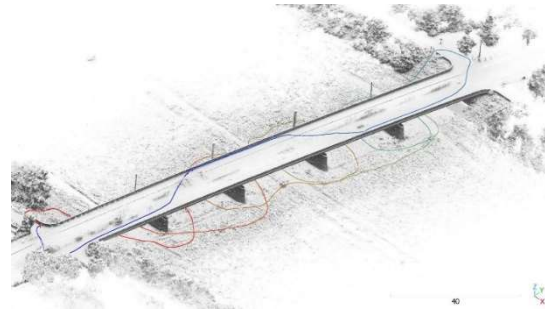

Figure 2. Captured PLS point cloud and trajectory

2.3 Personal laser scanner device

The PLS system used for the measurements was the GeoSlam ZEB Horizon, consisting of the scan head, the additional ZEB Cam and the data logger with battery pack (Figure 3). The system has a point measurement rate of 300,000 points/sec. with a distance measurement noise of ±30 mm. The maximum measurement distance is specified by the manufacturer as 100 m under optimal measurement conditions and 60-80 m under typical field conditions (ZEB Horizon User Guide). The geometric quality of the resulting 3D data depends on the length of the PLS paths. The maximum loop length recommended by the manufacturer is 30 minutes.

Figure 3. GeoSlam Horizon with attached ZEB Cam, data logger and battery pack

2.4 SLAM processing and georeferencing

The initial processing was carried out using the manufacturer's GeoSlam HUB software, which will also allow for the planned use of ZEB Cam image data for future investigations. The processing chain included SLAM processing, extraction of camera frames and final georeferencing. The result comprises the georeferenced point cloud, the image frames and the scanner and camera trajectories for each measurement made.

3. Method

This section presents the method for analyzing the PLS data segment by segment. This includes geometric feature based segmentation (Sec. 3.1), segment-based fine registration (Sec. 3.2), and point cloud deformation analysis (Sec. 3.3).

3.1 Geometric feature based segmentation

The first pre-processing steps were carried out in CloudCompare, starting with a coarse cropping to the bridge structure. Since the point density of a point cloud affects the computational time of neighborhood-based algorithms, the point cloud was subsampled

to 0.02 m spacing. In the next step, the Cloth Simulation Filter (CSF) developed by Zhang et al. (2016) was used to roughly remove all ground points from the dataset. The remaining ground points are automatically removed in the following segmentation process. In the final pre-processing step, the geometric feature verticality was calculated. This assigns a value to each point in a point cloud according to the spatial orientation of its nearest neighbors. The verticality according to Demantké et. al (2012) is computed as a vertical score using the following equation:

$$\text{Verticality}_{P_i} = 1 - \left| z_{\vec{e3}} \right|, \qquad (1)$$

with $z = 3^{\text{rd}}$ component of the normal vector
         $\vec{e3}$ = normalized vector of the structure tensor.

For each point P_i of the point cloud, the 3D structure tensor is calculated from the neighboring points within a radius of 0.10 m, resulting in three eigenvectors $\vec{e1}$, $\vec{e2}$, $\vec{e3}$, where $\vec{e3}$ corresponds to the normal vector. The verticality score for the point is calculated from the 3rd component $z_{\vec{e3}}$ of $\vec{e3}$. The verticality score takes values between 0 for points in horizontal areas and 1 for points in vertical areas. It is the basis for the further segmentation process.

The segmentation was implemented as a two-stage process. First, the entire point cloud was clustered with a minimum distance between points from different clusters adapted to the average point distance. The largest cluster was extracted including points from the bridge structure, adjacent vegetation, ground, and moving objects. The extracted cluster was then split into a horizontal part and a vertical part using the verticality score. In the second segmentation step the clustering was performed separately for the horizontal and the vertical part. The cluster sizes were determined using a histogram analysis. Clusters with a point count of less than 100,000 points result from vegetation, ground, and scatter points and have been removed. The remaining vertical clusters include the bridge pillars, side walls and bridge railings. Road surface, sidewalk surfaces, and the horizontal underside of the bridge can be found in the horizontal clusters.

3.2 Segment-based fine registration

The basis for the segment-based fine registration is an assignment of the segments extracted from the PLS and TLS data. Please note, that the number and the extent of the extracted segments can vary between PLS and TLS datasets due to the different resolution and measurement noise. At the current stage of the research, this problem had to be solved manually. Subsequently, a centroid-based automatic assignment of TLS and PLS segments is possible.

The assigned segments were then fine-registered in pairs using a point-to-point based iterative closest point (ICP) algorithm based on the work of Besl et. al (1992). The TLS point cloud was used here as a non-deformed reference to evaluate the PLS dataset for deviations. The first step is to register all individual segments. This is followed by the logical merging of segments with little spatial structure into combined segments. The result are the parameters of the transformation matrix calculated by ICP, consisting of the rotation angles ω, ϕ and κ around the coordinate axes and the translation components t_X, t_Y and t_Z in the respective coordinate direction. If the 3D point cloud to be analyzed is not deformed and free from systematic deviations, the parameters determined for each segment pair should be identical. Conversely, parameter differences between segment pairs indicate displacements within the PLS point cloud.

3.3 Point cloud deformation analysis

After fine registration using ICP, the remaining deviations between the PLS point cloud and the TLS control point cloud can be calculated. Each segment can be analyzed for any deformations existing within the limits of the registration accuracy achieved. Several methods are available to determine the distance values. For example, the distance can be calculated directly between the nearest neighbors of two point clouds using the cloud-to-cloud method, or between a point cloud and a mesh. These methods have been successively improved and adapted to different use cases. There are several variants, including local modelling of the object surface for more accurate distance calculation, or the use of an existing 3D model instead of a meshed surface. With the M3C2, Lague et. al (2013) developed a multiscale model-to-model cloud comparison method, which does not require meshing of the surface and includes the 3D surface variation. It is therefore particularly suitable for natural structures with partially dynamic subareas. For the deformation analysis of the PLS point clouds carried out here, the computation of the point-to-point distance is performed with a local modelling of the surface over the nearest neighbors. For the rigid surface of the bridge, a more complex variant such as the M3C2 method is not required.

4. Results and discussion

4.1 Georeferencing PLS Data

For georeferencing a rigid transformation was performed, which does not involve any reprocessing of the SLAM. The distribution of the control points (CP_1 to CP_4) used for georeferencing is shown in Figure 4. The points are located along the trajectory at the upper level of the road. The spatial distribution is not optimal as all the points are at road level and arranged almost in a line. The results of the rigid transformation are summarized in Table 1. The residuals in the range of up to one decimeter can be explained by the measurement conditions. Stable SLAM processing requires a high coverage of the scanner field of view with rigid objects that are as planar as possible. This is usually difficult to achieve when measuring a free-standing bridge. As can be seen in Figure 4, there are no rigid objects next to the bridge.
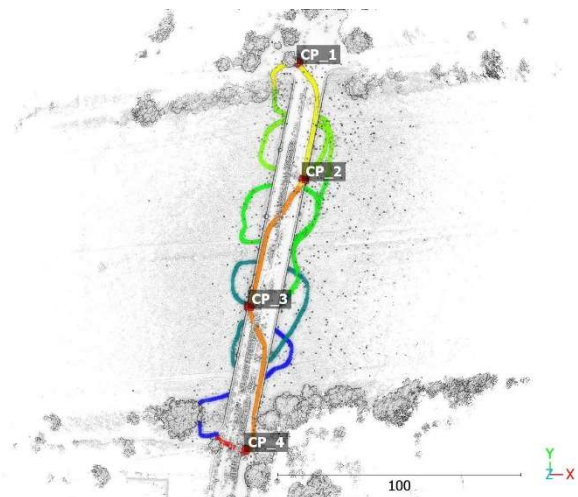

Figure 4. Top view of the captured PLS point cloud with the measurement trajectory and the control points

In addition, the ground consists of a highly dynamic grass surface of approximately 0.5-1 m height. In order to minimize the lack of

fixed structures outside the bridge, sub-loops were walked around the bridge pillars. These have the potential to partially compensate for the above disadvantages. At street level, there were no stabilizing surfaces other than the bridge itself. In addition, the repetitive character of the bridge railing has an unfavorable effect on the stability of the SLAM computation.

Name	dx	dy	dz	Error
	m	m	m	m
CP_1	-0.008	-0.072	0.061	0.095
CP_2	-0.003	-0.016	-0.042	0.045
CP_3	-0.006	-0.002	-0.086	0.086
CP_4	0.017	0.089	0.069	0.114
			RMS [m]	0.085

Table 1. Results of the rigid transformation in GeoSlam HUB

The obtained average RMS of 0.085 m is sufficient as a coarse registration for the subsequent PLS to TLS point cloud fine registration.

4.2 Geometric feature based segmentation

The following section summarizes the results of the segmentation process. Since the approach was identical for the TLS and PLS datasets, only the PLS results are presented. Figure 5 (top) shows the initial point cloud after coarse cropping, sub-sampling and coarse removal of the ground points with CSF.
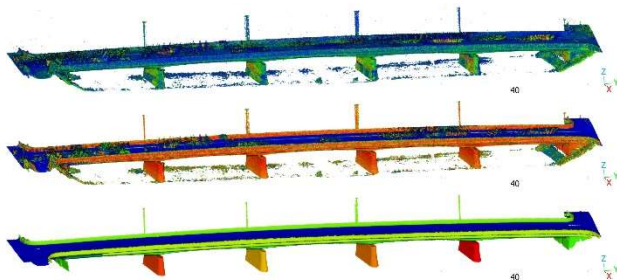

Figure 5. Intermediate and final result of the point cloud segmentation. Coarsely cleaned initial point cloud color coded by intensity (top), initial point cloud colored by verticality (center) and final cleaned and segmented point cloud (bottom)

In the next step the vertical score was computed. For this purpose, a value for the search radius had to be determined in order to compute the 3D structure tensor. An analysis of the surface point density showed areas of lower density for the PLS measurement on the road surface. Therefore, the search radius was set to 0.10 m for both data sets. The point cloud colored by the verticality is shown in Figure 5 (center). Horizontal areas with values between 0 and 0.1 are blue, vertical areas with values between 0.7 and 1 are red. The respective acceptance ranges were determined after analyzing the score for differently oriented surfaces and curvatures. With a delta of 0.3, the vertical acceptance range is larger than the horizontal. Due to the outward curvature of the bridge pillars, the vertical range had to be chosen larger so that no pillar points were excluded. The total point cloud, enriched with the vertical score and coarsely cleaned, was then divided into vertical and horizontal segments in a two-stage segmentation process.

The first segmentation process was carried out with a threshold of 0.1 m, adapted to the point cloud density. Only the largest point cluster was kept as it contained the bridge structure. The computed vertical score was then used to split the total point cloud into vertical surface points and horizontal surface points. Points with a score in the intermediate range [0.11 to 0.69] were excluded. This range includes points at surface transitions such as curb lines or rounded edges. Removing these points results in a loss of detail, but increases separability during the second segmentation process. It has been done separately for horizontal and vertical areas.

In order to obtain an optimal result, the cluster segmentation threshold for the vertical components was empirically reduced to 0.075 m, while the value for the horizontal components remained unchanged with respect to the first segmentation step. After the second segmentation, the cluster sizes were determined using a histogram analysis. All clusters with a point count of less than 100,000 points were removed.

As already described in section 3.2, the segmented clusters can vary in number and characteristics. In this study, 15 clusters were segmented for the TLS data set and 13 for the PLS data set. Method-specific characteristics, such as different levels of measurement point noise, result in a lack of separation between the railing and the underlying side wall for the PLS measurement (Figure 6 right in green). In the case of the TLS measurement, these two components could be separated (Figure 6 left in blue and red). Therefore, manual post-processing and assignment had to be carried out here. In the PLS data set, the side railings and the underlying vertical side wall were manually separated from each other so that the clusters match the TLS data.
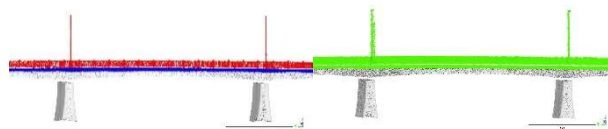

Figure 6. Railing and side wall as two separate clusters in the TLS data set (left) and as one cluster in the PLS data set (right)

The final segmented point cloud is shown in Figure 5 (bottom), colored according to the cluster ID. Figure 7 shows the segmentation results on a profile. It is obvious that measuring points caused by passing vehicles were also removed in the course of segmentation.
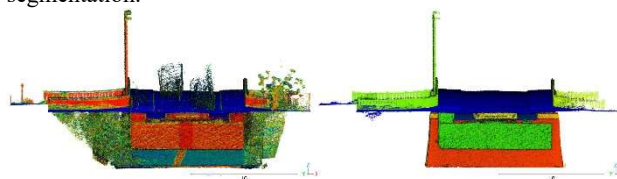

Figure 7. Initial point cloud colored by verticality (left) and final segmented point cloud colored by cluster ID (right)

In the case of the PLS measurement, the absolute number of points has been reduced from 10.5 M points to 8.8 M points. However, this also includes points on the bridge surface that were removed by the clustering in areas where the distance between points was too high or where there was partial occlusion. The number of points in the TLS measurement was reduced from 12.2 m. points to 9.2 m. points using the same procedure.

After segmentation, all segments were given an ID, as shown in Figure 8. This ID is used to identify the horizontal segments (h1-h5) and vertical segments (v1-v10) in the following steps.
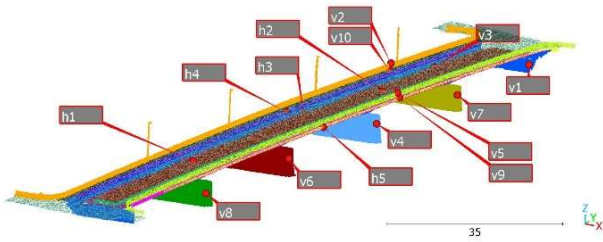
Figure 8. Labelled point cloud segments

4.3 Segment-based fine registration

Segmentation and subsequent post-processing provides 5 horizontal and 10 vertical segments for both TLS and PLS point clouds, which are roughly registered to each other via georeferencing. Fine registration is carried out segment by segment using ICP. The functionality of the method is first examined on synthetically transformed TLS data, which do not exhibit any geometric deformations. It is then applied to the PLS data, where the result of the fine registration may be affected by existing point cloud deformations. The following tests are carried out in detail:

- Fine registration of original TLS segments with synthetically shifted TLS segments

- Fine registration of original TLS segments with synthetically shifted and rotated TLS segments

- Fine registration of TLS segments with PLS segments

- Fine registration of combined TLS segments with combined PLS segments

The results of the tests are presented below. The directional vectors of the transformation parameter sets are shown graphically for visualization purposes. The vector visualization is scaled for better visibility. The elements of the transformation consisting of the three rotational elements ω, ϕ, κ and the three translational elements t_X, t_Y, t_Z, are displayed segment by segment in numerical form.

For the first test, the TLS point cloud was duplicated and synthetically transformed. Initially, no rotation was performed, only a translation. The computation of the fine registration for all individual segments was performed with an average RMSE of 5.3E-6 m. As can be seen from the summary in Table 2, all individual computations produce identical transformation parameters. The translation vectors shown in Figure 9 also indicate an identical translation of the segments.

ID	ω	ϕ	κ	t_X	t_Y	t_Z
	°	°	°	m	m	m
h1	0.000	0.000	0.000	-0.100	0.350	-0.400
…	…	…	…	…	…	…
h5	0.000	0.000	0.000	-0.100	0.350	-0.400
v1	0.000	0.000	0.000	-0.100	0.350	-0.400
…	…	…	…	…	…	…
v10	0.000	0.000	0.000	-0.100	0.350	-0.400

Table 2. Transformation parameters resulting from the fine registration of synthetically shifted TLS segments to original TLS segments.
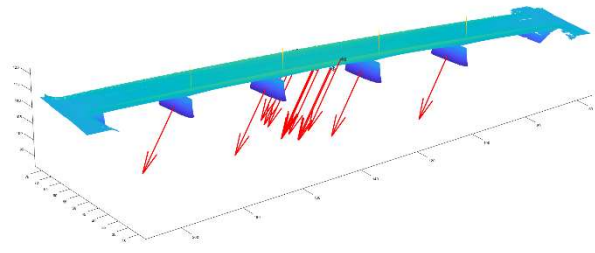

Figure 9. Translation vectors resulting from the fine registration of synthetically shifted TLS segments to original TLS segments.

For the second test, the TLS point cloud was again duplicated and synthetically transformed. The transformation parameters were derived from a preliminary registration of the TLS point cloud to the PLS point cloud in order to represent a more realistic scenario. In addition to a translation, this also includes rotations around XYZ axis. The translation vectors of the individual segments initially show a comparable alignment on a visual level (Figure 10).
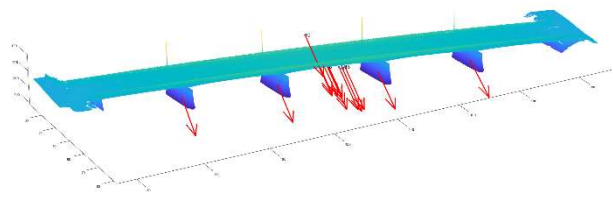

Figure 10. Translation vectors resulting from the fine registration of synthetically shifted and rotated TLS segments to original TLS segments

With an RMSE of 0.010 m, the fine registration for the horizontal segments h1, h2 and h3 is less accurate than for the other horizontal and vertical elements (h4-v10). With an RMSE of 8.5E-6 m, their accuracy was comparable to the results of the first test. The lower registration accuracy of h1, h2 and h3 can also be seen in the transformation parameters summarized in Table 3, which differ from the values for h4 to v10. The most significant difference occur with the rotation angle ω and the translation parameters t_X and t_Y. The deviations can be explained by the shape of the segments, which are almost flat with only a light curvature.

ID	ω	ϕ	κ	t_X	t_Y	t_Z
	°	°	°	m	m	m
h1	**0.0039**	**-0.1024**	-0.0218	**0.190**	**-0.042**	-0.044
h2	**0.0047**	**-0.1023**	-0.0217	**0.192**	**-0.042**	-0.044
h3	**0.0031**	-0.1027	-0.0218	**0.189**	**-0.040**	-0.045
h4	0.0242	-0.1028	-0.0218	0.238	-0.060	-0.045
h5	0.0242	-0.1028	-0.0218	0.238	-0.060	-0.045
v1	0.0242	-0.1028	-0.0218	0.238	-0.060	-0.045
…	…	…	…	…	…	…
v10	0.0242	-0.1029	-0.0218	0.238	-0.060	-0.045

Table 3. Transformation parameters resulting from the fine registration of synthetically shifted and rotated TLS segments to original TLS segments.

The third test involved registering the PLS segments to the TLS segments. Due to the higher point noise of the PLS data compared to the TLS point cloud, higher RMSE values were expected for the fine registration. However, the RMSE values proved to be too high for some segments. In particular, the separate fine

registration of railings, horizontal undersides or sidewalls proved to be too error-prone. The vertical railing elements v2 and v5 (RMSE 0.126 m) and the underlying side surfaces v9 and v10 (RMSE 0.155 m) are listed here as examples.

ID	ω	φ	κ	t_X	t_Y	t_Z
	°	°	°	m	m	m
v2	0.068	-0.677	-0.151	1.547	-0.212	-0.251
v5	0.382	12.613	2.761	-24.55	2.840	9.309
v9	0.290	10.272	2.452	-21.16	-2.679	6.671
v10	0.106	4.611	0.881	-8.564	3.356	1.975

Table 4. Exemplary results of ICP rotation angles and translation. Original TLS dataset to PLS dataset

The registration problems are also reflected in the transformation parameters of the individual segments summarized in Table 4. The rotation and translation values are very high and do not match the coarse registration.

The results of test 3 show that the extracted segments are unsuitable for segment-based fine registration. In order to achieve greater stability for the fine registration, segments were therefore combined in the fourth test. The temporal measurement sequence and the trajectory are taken into account. The combined segment c1 consists of the horizontal road and pavement surface located at the top and the two vertical railing segments. Segment c2 contains the horizontal bottom segments measured only from below and c3 is the combination of the vertical bottom segments and the vertical end walls at the level of the two abutments. The pillar segments v4, v6, v7 and v8 remain unchanged.

The fine registration RMSE of the combined segment c2 and all pillar segments (v4, v6, v7, v8) were on average 0.022 m. With a value of 0.034 m, the RMSE of c3 was higher, which can be explained by the low coverage of points in the southeastern part of the PLS point cloud. This resulted in a lower degree of overlap for this segment. With an RMSE of 0.061 m, c1 has the lowest fitting accuracy. Possible explanations for this are the high point noise of the handrail segments, but also possible deformations within the segment. This is analyzed in more detail in Section 4.4.
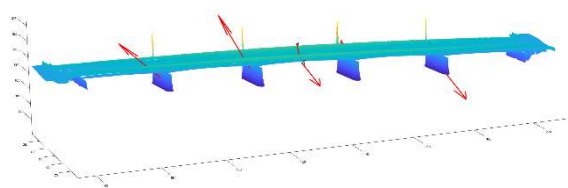

Figure 11. Translation vectors resulting from the fine registration of combined PLS segments to combined TLS segments

ID	ω	φ	κ	t_X	t_Y	t_Z
	°	°	°	m	m	m
c1	0.0259	-0.0026	0.0047	0.058	-0.011	-0.027
c2	0.0125	-0.0208	-0.0006	0.059	-0.009	0.009
c3	0.0223	-0.0639	-0.0043	0.150	-0.007	-0.026
v4	0.0075	0.0370	-0.0012	-0.080	0.011	0.051
v6	0.0119	0.0339	-0.0463	-0.055	-0.066	0.142
v7	0.0152	0.0861	0.0807	-0.160	0.145	-0.147
v8	0.0149	-0.0279	-0.0834	0.077	-0.126	0.117

Table 5. Results of ICP rotation angles and translation. Original TLS dataset to PLS dataset (combined)

The transformation parameters of the fourth test, summarized in Table 5, show differences in both rotation and translation. Note that the absolute values of the rotation angles are at a relatively low level.

As can be seen in the vector representation of the translation parameters in Figure 11, they do not show a homogeneous alignment. This is particularly evident for the pillar segments v4, v6, v7 and v8. These segments are partially shifted in opposite directions, both laterally and vertically. Taking into account the higher point noise in the PLS point clouds, the values indicate shifts within the PLS point cloud.

4.4 Point cloud deformation analysis

To validate the results of the fine registration and to analyze potential geometric deformations in the PLS point clouds, the cloud-to-cloud (C2C) distances were calculated for the combined segments c1-c3 and the pillar segments v4, v6, v7 and v8. A local modelling based on the 6 nearest neighbors was used. The TLS segments served as reference. Calculation, analysis and visualization are carried out using the CloudCompare Software.

Since the results for the combined segments are very similar, they are only presented for c1. Figure 12 shows the corresponding C2C distances. As the analysis of the horizontal road surface was expected to show the most significant deviations in the height direction, the point cloud is colored according to the Z-component of the C2C values. Obviously, the distances across the road surface are not constant, but show a trend. In the area of the abutments, the distances are between 0 and -0.10 m, while in the center of the bridge, the values are between 0.05 m and 0.10 m.
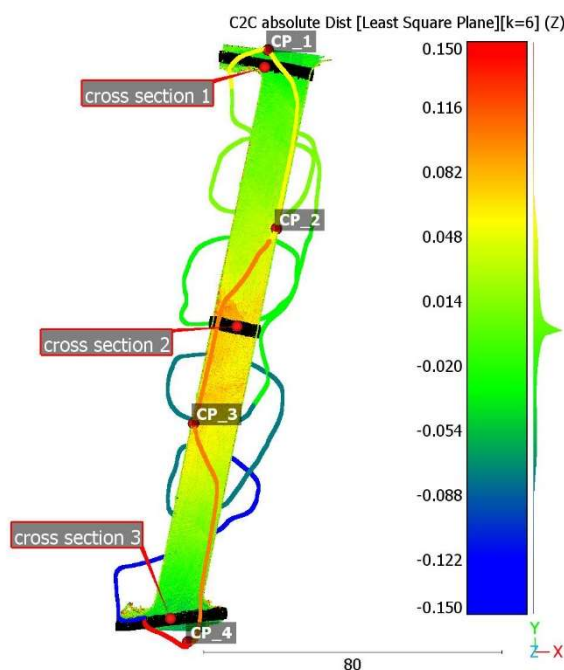

Figure 12. Combined segment c1 colored by Z-component of C2C distances with control points (CP_1 to CP_4), PLS trajectory color-coded according to time, and cross sections cs1-cs3.

For a more detailed analysis of the systematic-errors, profiles were extracted in areas of interest and the distances were statistically analyzed. For this purpose, a histogram fit of a Gaussian distribution was performed. The position of the profiles is shown

in Figure 12. The mean values and standard deviations of the C2C distances are presented in Table 6.

ID	$\bar{x}_{dZ}$	s_{dZ}
	m	m
cs1	-0.053	0.012
cs2	0.055	0.016
cs3	-0.071	0.015

Table 6. Mean values ($\bar{x}_{dZ}$) and standard deviations (s_{dZ}) of cloud-to-cloud distances in height direction

The PLS points in the abutment areas (cs1 and cs2) are on average 5-7 cm below the TLS points. The PLS points in the center of the bridge (cs3) tend to be an average of 5.5 cm higher than the reference point cloud. No direct correlation can be made between the trend observed here and the control points CP_1 to CP_4 as well as the PLS trajectory shown in Figure 12. Only an increased point density in the proximity of the trajectory and in the areas of the stationary measured control points can be seen, but without a directly detectable influence on the differences shown here.

In the analysis of the C2C distances of the pillar segments the lateral X and Y components are considered separately. As can be seen in Table 7, the deviations for all 4 pillars are normally distributed centered around zero, with a proportion of around 98 % of the points in the X direction (Pts_{dX}) scattering in the range of ±0.02 m and in the Y direction (Pts_{dY}) in the range of ±0.05 m.

ID	$\bar{x}_{dX}$	Pts_{dX} in ±0.02 m	s_{dX}	$\bar{x}_{dY}$	Pts_{dY} in ±0.05 m	s_{dY}
	m	%	m	m	%	m
v4	0.0	97.9	0.006	0.0	98.5	0.017
v6	0.0	98.3	0.007	0.0	98.7	0.017
v7	0.0	98.4	0.006	0.0	98.2	0.018
v8	0.0	98.3	0.006	0.0	98.7	0.017

Table 7. Mean values ($\bar{x}_{dX}$ $\bar{x}_{dY}$) and standard deviations (s_{dX} s_{dY}) of cloud-to-cloud distances in lateral directions

There are noticeable trends in the calculated distances both in the X-direction (Figure 13) and in the Y-direction (Figure 14). The RMSE values of the fine registration (Section 4.3), which are uniformly low for all pillars, indicate that there is no residual registration error. A scale error could also be excluded by a test calculation with additional scale estimation.

Therefore, external influences such as environmental conditions or the measurement path remain as possible causes for a locally increased measurement point noise. Due to the sub-loops around the pillars, there are surface areas that were mapped from different distances and incidence angles. The differing transformation parameters indicate a displacement of the pillars in relation to the overall bridge system, but no significant inner-segment deformations could be derived from the C2C distances.
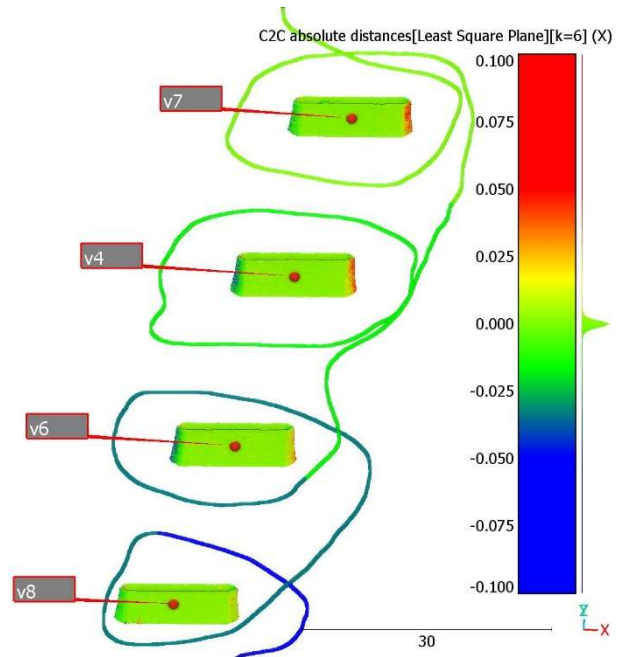

Figure 13. Pillar segments v4, v6, v7 and v8 colored by X-component of the C2C distances
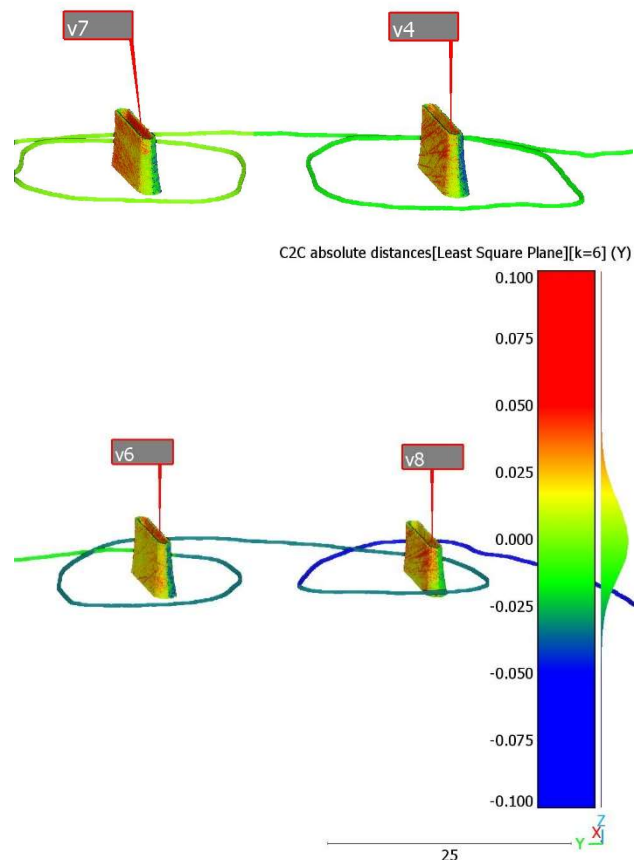

Figure 14. Pillar segments v4, v6, v7 and v8 colored by Y-component of the C2C distances

5. Conclusion and outlook

This study presents a method for analyzing geometric displacements or deformations in PLS point clouds in the context of the geometry acquisition of bridge structures. The basic idea is a segment-by-segment comparison of the PLS point cloud with TLS reference data. For this purpose, a geometric feature based segmentation is performed first. The resulting segments are then registered in a segment-based fine registration. Finally, the deformations of the PLS point cloud are analyzed in a point cloud comparison. However, some segments were not suitable for a segment-based analysis due to their characteristic shape. By combining these segments into groups, an evaluation was still possible. For example, the combination of the road surface and the side railing has resulted in a more stable registration.

The results of the segment-based ICP fine registrations already indicate the presence of local displacements within the PLS point cloud due to varying transformation parameters. In the subsequent C2C distance analysis, a deformation in the road geometry was detected. However, no significant internal segment deformations were observed in the pillar segments. The normal distribution of the C2C distances for all pillar segments confirms the good average registration accuracy. Overall, it could be shown that local deformations or component shifts can be detected with the proposed method.

In future studies, we will consider the quality of the computed trajectory and the point density of the PLS systems, which show local variations depending on the recording configuration. In this way, inaccuracies with respect to the SLAM condition can be analyzed and possible correlations can be identified. Moreover, the time stamps contained in the PLS point clouds can be used in the future as alternative parameter for segmenting the data. In addition to the comparisons between PLS and reference point clouds performed here, future work should also include the determination of values such as component thickness or component spacing and their validation against in-situ reference values. In this way, compliance with measurement tolerances can also be validated. Based on these adaptations, strategies to improve point clouds generated by PLS systems will be developed and implemented.

References

Aricò, M., La Guardia, M., Lo Brutto, M., Rappa, E. M., Vinci, C., 2023. Mobile Mapping for Cultural Heritage: the Survey of the Complex of ST. John of the Hermits in Palermo (italy). *The International Archives of the Photogrammetry, Remote Sensing and Spatial Information Sciences,* 48, 25-32.

Besl, P. J., McKay, N. D., 1992. Method for registration of 3-D shapes. *Sensor fusion IV: control paradigms and data structures* (Vol. 1611, pp. 586-606). Spie.

Blaskow, R., Eltner, A., 2023. Investigation of the Suitability of a Personal Laser Scanning Device for the Monitoring of Small Water Bodies. *The International Archives of the Photogrammetry, Remote Sensing and Spatial Information Sciences*, 48, 45-50.

Demantké, J., Vallet, B., Paparoditis, N., 2012. Streamed vertical rectangle detection in terrestrial laser scans for facade database

production. *ISPRS Annals of the Photogrammetry, Remote Sensing and Spatial Information Sciences,* 1, 99-104.

Haslbeck, M., Strübing, T., Braml, T., 2022. Quantification of Uncertainties for Geodetic Observations in the Context of Bridge Surveillance. *In Proceedings of the 1st Conference of the European Association on Quality Control of Bridges and Structures: EUROSTRUCT 2021* 1 (pp. 1-13). Springer International Publishing.

Huang, L., 2021. Review on LiDAR-based SLAM techniques. In *2021 International Conference on Signal Processing and Machine Learning (CONF-SPML)* (pp. 163-168). IEEE.

Lague, D., Brodu, N., Leroux, J., 2013. Accurate 3D comparison of complex topography with terrestrial laser scanner: Application to the Rangitikei canyon (NZ*). ISPRS Journal of Photogrammetry and Remote Sensing,* 82, 10-26.

Mader, D., Blaskow, R., Westfeld, P., Maas, H. G., 2015. UAV-based acquisition of 3D point cloud – a comparison of a low-cost laser scanner and SFM-tools. *The International Archives of the Photogrammetry, Remote Sensing and Spatial Information Sciences,* 40, 335-341.

Mandlburger, G., Pfennigbauer, M., Schwarz, R., Flöry, S., Nussbaumer, L., 2020. Concept and performance evaluation of a novel UAV-borne topo-bathymetric LiDAR sensor. *Remote Sensing*, 12(6), 986.

Poku-Agyemang, K. N., & Reiterer, A., 2023. 3D Reconstruction from 2D Plans Exemplified by Bridge Structures. *Remote Sensing,* 15(3), 677.

Previtali, M., Brumana, R., Banfi, F., 2022. Existing infrastructure cost effective informative modelling with multisource sensed data: TLS, MMS and photogrammetry. *Applied Geomatics,* 14(Suppl 1), 21-40.

Sardemann, H., Blaskow, R., Maas, H. G., 2023. Camera-Aided Orientation of Mobile Lidar Point Clouds Acquired from an Uncrewed Water Vehicle*. Sensors*, 23(13), 6009.

Tupinambá-Simões, F., Pascual, A., Guerra-Hernández, J., Ordóñez, C., de Conto, T., Bravo, F., 2023. Assessing the Performance of a Handheld Laser Scanning System for Individual Tree Mapping – A Mixed Forests Showcase in Spain. *Remote Sensing*, 15(5), 1169.

Zhang, W., Qi, J., Wan, P., Wang, H., Xie, D., Wang, X., Yan, G., 2016. An easy-to-use airborne LiDAR data filtering method based on cloth simulation. *Remote Sensing,* 8(6), 501.